Research Article Vol. 29, No. 7 / 29 March 2021 / *Optics Express* 10939

Optics EXPRESS

Temperature-independent ultra-sensitive refractive index sensor based on hollow-core silica tubes and tapers

SHUN WU,[1] HAIHAO CHENG,[1] JIANWEN MA,[1] XUEMEI YANG,[1] SHUN WANG,[1,*] AND PEIXIANG LU[1,2]

[1] *Hubei Key Laboratory of Optical Information and Pattern Recognition, Wuhan Institute of Technology, Wuhan 430205, China*
[2] *School of Physics and Wuhan National Laboratory for Optoelectronics, Huazhong University of Science and Technology, Wuhan 430074, China*
[*] *shunwang@wit.edu.cn*

Abstract: We demonstrate a simple and ultra-sensitive refractive index (RI) sensor using a hollow-core silica tube (HCST) sandwiched between an up-taper and a down-taper in single mode fibers (SMF). According to our theoretical analysis, the interference spectrum comes from a combination of a three-beam multi-mode interference and anti-resonance effects. RI sensing will affect the mode interference. By demodulating the fringe contrast of the interference spectra, an ultrahigh sensitivity of -120.18 dB/RIU is achieved, implying a RI resolution of $\sim 8\times10^{-6}$ in the RI range from 1.35 to 1.43. What's more, the sensor has great temperature insensitivity of -0.0085 dB/°C, indicating an extremely low cross sensitivity of 7×10^{-5} RIU/°C, which further benefits its practical application. The proposed configuration does not require special fiber or fabrication technique. In addition, the sensor's other merits such as simple and compact structure and ease offabrication offer the potential in biochemical sensing applications.

1. Introduction

RI is the basic physical characteristics of materials, revealing important information such as quality, composition, and content in goods, which offers great importance for RI measurement. In the past decades, various types of optical fiber sensors(OFS) for RI measurement have been studied and demonstrated in the fields of biological analysis [1,2], chip science [3,4], gas sensing [5–7], and etc. Based on sensing principles, they can be divided into different categories such as fiber gratings, including fiber Bragg grating (FBG) [8], long period grating (LPG) [9] and tilting grating [10], Surface Plasmon Resonance (SPR) [11,12], interferometer type involving Mach-Zehnder Interferometers (MZI) [13], Michelson Interferometers (MI) [14], Fabry–Pérot interferometer (FPI) [15] and Sagnac interferometer (SI) [16]. With the development of fiber-based RI sensing, a lot of applications based on interferometer type have been promoted for biochemical properties measurement such as PH value [17], DNA [18], sugar [19], humidity [20], temperature [21], and etc.

According to the detection signal, the RI sensors can be demodulated by intensity [22], wavelength [8–10], and phase [11–16]. To improve the detection performance and open up new ideas for RI sensor, many novel sensing structures have been reported in the past three years. C. Jiang *et. al.* [23] proposed and verified helical long-period gratings(HLPG) inscribed in polarization-maintaining fibers by CO_2-Laser, and an RI sensitivity of 7248.6 nm/RIU in 1.4470-1.4600 RIU range was obtained. Z. Zhang *et. al.* [24] used broadband cladding mode coupling mediated by a tilted fiber Bragg grating (TFBG) and an in-fiber mirror, achieving a sensitivity of 528 nm/RIU from 1.33 to 1.41 RIU. Q. Wang *et. al.* [25] proposed a sensor that coating indium tin oxide (ITO) layer immobilized onto the Cu film. An ultrahigh sensitivity

#422701 https://doi.org/10.1364/OE.422701
Journal © 2021 Received 17 Feb 2021; revised 10 Mar 2021; accepted 12 Mar 2021; published 23 Mar 2021

of 4583.4 nm/RIU was achieved. Other newly reported novel RI sensors are demodulated by intensity of fringe dips. For example, our previous work [22] reported and demonstrated a highly-sensitive RI sensor based on a linear-cavity dual-wavelength erbium-doped fiber laser. Thanks to the dual-wavelength gain competition mechanism, a high sensitivity of 231.1 dB/RIU from RI range of 1.300 to 1.335 is obtained.

In general, these wavelength or phase type RI sensors have advantages such as high sensitivity and simple principle, but also have various disadvantages. For example, the HLPG and TFBG configurations require special laser writing, while ITO-Cu structure requires coating process, which increase the complexity and production cost. Furthermore, one essential element for certain in-line interference configurations is special fiber, such as multi-core fiber, partial core optical fiber, twin-core fiber, and etc., which is sometimes difficult to obtain. To solve this problem, researchers have made a lot of effort to create novel RI sensing structures. J. Kang *et. al.* [26] proposed an RI sensor based on the front-tapered single-mode-multimode-single-mode (FT-SMS) fiber structure, whose relative sensitivity is −342.815 dB/RIU in the range of 1.33~1.37. M. Shao *et. al.* [27] demonstrated a MZI based single-mode-thin-core-multimode-single-mode (STMS) fiber structure for RI measurement. By exposing the cladding of multimode fiber after hydrofluoric (HF) acid corrosion, the RI sensitivity in intensity form reached 112.37 dB/RIU. In spite of high sensitivity, HF acid is toxic to humans and the fabrication process is relatively complex.

In this paper, an inline RI sensor consisting of a hollow-core silica tube sandwiched between SMF tapers is demonstrated. By applying the beam propagation method (BPM), our simulation implies that a three-beam interference pattern can be formed involving the core mode, the reflected core mode, and the excited cladding mode. The simulation also reveals that when the external RI varies, the intensity of the excited cladding mode would alter leading to the change on the fringe contrast of the interference spectrum. Therefore, RI sensing can be realized by demodulating the fringe contrast of this multi-mode interference spectrum. Our experimental results confirmed the theory, and showed an ultrahigh RI sensitivity of -120.18 dB/RIU in the RI range from 1.35 to 1.43. Furthermore, this sensor has a low temperature sensitivity of -0.0085 dB/°C, which indicates extremely low cross sensitivity of 7×10^{-5} RIU/°C. Besides, this sensor's advantages such as simple, compact and easy to manufacture further benefit its biochemical sensing applications.

2. Sensor principle and simulation

The schematic diagram of the proposed sensor structure is shown in Fig. 1(a). A segment of hollow-core silica tube (HCST) is spliced between two pieces of SMFs. The two splicing interfaces form a low finesse cavity. When light goes through the waist of the SMF down-taper, multiple cladding modes will be excited due to mode field mismatch. As the core mode propagates along the core of the silica tube, it will be reflected back and forth inside the cavity. Due to the structural loss in HCST, the intensity of the high-order cladding modes and multiple reflected beams are greatly reduced and can be ignored. Therefore, all beams in the structure are simplified into three beams: the core beam, the low-order cladding beam, and the core beam after being reflected twice. Due to the optical phase difference (OPD) among those beams, a typical three-beam interference is formed.

In order to analyze the light propagation characteristics of the sensor structure, we utilized the beam propagation method (BPM) to simulate the light energy distribution inside the sensor. In the simulation, the length of HCST is 6 mm. The RI values of the ambient, the core, as well as the cladding RIs of HCST and SMF are set to 1, 1.45205 and 1.44681, respectively. Figure 1(b) shows how the intensity of light travelling in the core varies as it propagates along the fiber under different external RIs. We can see that the light is tightly bound in the core at first. When it passes through the down-taper, a small part of the light in the core is coupled to the evanescent field, resulting in abrupt loss of intensity. After that, light will be coupled back to the core or

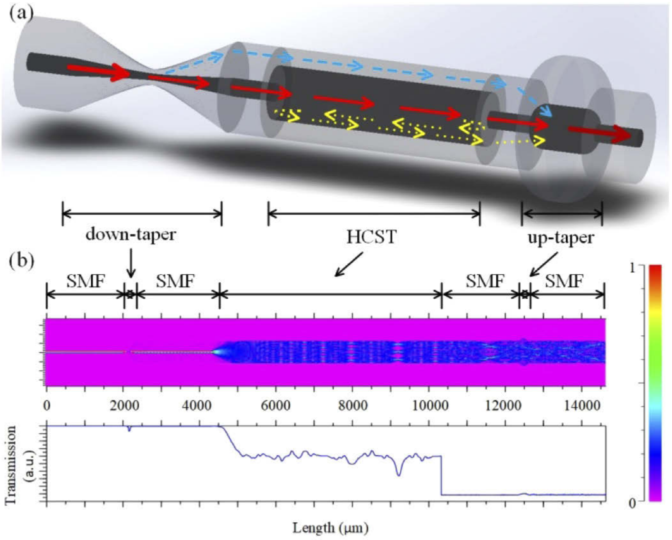

Fig. 1. (a) Schematic diagram of our sensor structure; (b) Light energy distribution inside the sensor based on BPM simulation when the external RI is 1.

cladding and continue to propagate forward. Owing to the special waveguide structure of the HCST, part of the light leaks out to the cladding of HCST, anti-resonant effect (ARE) occurs when the resonance condition is satisfied [28]. At the second interface between the HCST and SMF, only a small amount of the light is coupled back into the core and cladding of the SMF again. The beam energy decreases sharply because of the air core of the HCST is 7.5 times larger than that of the SMF. The next up-taper is applied to recouple light back into the core and cladding of the leading-out SMF again. Thus, multi-beam interference occurs.

Figure 2 shows the simulation result of the change in the light intensity of the fiber core with external RI. The red dotted box around the up-taper represents the energy involved in the interference. It can be found that when the external RI is greater than 1 (sensor in liquid), some light in fiber core leaks outside, leading to the decrease in the light intensity. With the external RI increasing from 1.35 to 1.45, part of the light is coupled back into the core, and the light intensity in the fiber core gradually increases.

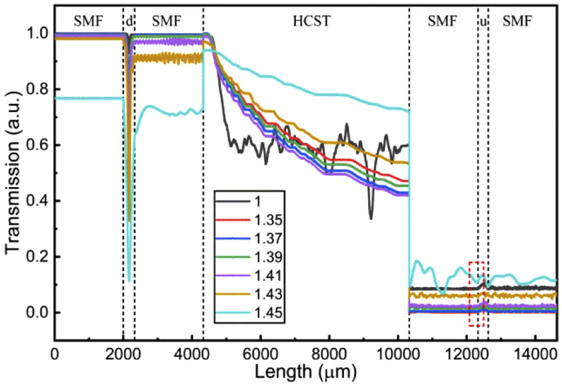

Fig. 2. The results of the energy distribution in fiber core simulated by BPM, during the external RI changes from 1.35 to 1.45. “d” and “u” represent “down-taper” and “up-taper”, respectively.

Based on the calculated intensity variation for the fiber core, we also simulated the change in the interference pattern with external RI, as shown in Fig. 3 (a). To simplify the numerical calculation, we only consider the real part of the electric field amplitude, and treat the complex amplitude as a constant. As the external RI changes from 1.35 to 1.39, and finally 1.43, the interference fringe contrast gradually decreases. The corresponding variation in the fringe contrast with external RI is displayed in Fig. 3(b). It can be seen that the core power gradually increases as the external RI changes from 1.35 to 1.45. The cladding power, which is slightly larger than the core power, increases faster than the core power until the external RI approaches 1.45, the RI of silica glass. Since the fringe contrast of an interference pattern is largely determined by the intensity of both beams involved in the interference, here we try to explain the contrast change by the core and cladding intensity simulation. Both intensities are about to be equal when the RI is 1.35. Then the intensity difference becomes larger until the external RI reaches 1.45. Therefore, the overall trend of the contrast is obtained by subtracting the minimum intensity from the adjacent maximum intensity, as shown in the inset figure in Fig. 3(b). We can see that the contrast decreases with the external RI from 1.35 to 1.43, then increases from 1.43 to 1.45. The sensitivity for the contrast variation due to RI change is estimated to be -145 dB/RIU.

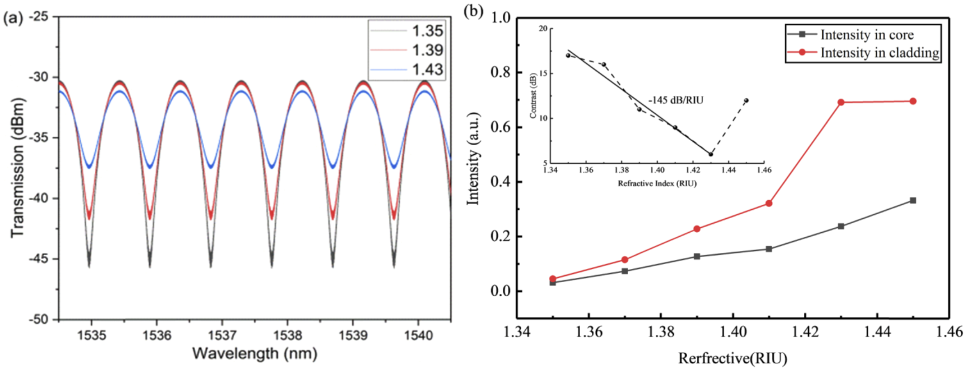

Fig. 3. (a) The simulated spectra obtained from the numerical calculation of the energy in the fiber core and cladding from Fig. 2; (b) The contrast results of the interference peak near 1538 nm.

3. Experimental results and discussion

3.1. Sensor fabrication

The proposed sensing structure is shown in the Fig. 1(a). It is fabricated by introducing a segment of 6 mm HCST sandwiched between a down-taper and an up-taper SMF. The length of the HCST was optimized based on the transmission spectra discussed in our previous work [29]. The core/cladding diameters of SMF (YOFC Ltd.) and HCST (Polymicro Technologies Ltd.) are 8/125µm and 75/125µm, respectively. Their cross-sectional microscopic pictures are shown in Fig. 4(a) and (b). The tapers and splicing between SMF and HCST are fabricated by commercial fusion splicer (Fujikura FSM-80S).

The three-step fusion process is shown in Fig. 5(a)-(c). All parameters for making the SMF up-taper, down-taper, and splicing SMF to HCST is listed in Table 1. An important step of making dumbbell-shape up-taper is to increase the amount of overlap during the fusion splice. Large overlap results in large mode field mismatch, which is in favor of the cladding mode excitation. So we used the maximum overlap setting allowed by the fusion splicer and obtained an up-taper waist of 160.47µm, with length of 302.33µm. The down-taper is realized by continuing the arc discharge, and tapering the structure after the SMF-SMF splice. SMF down-tapers of different

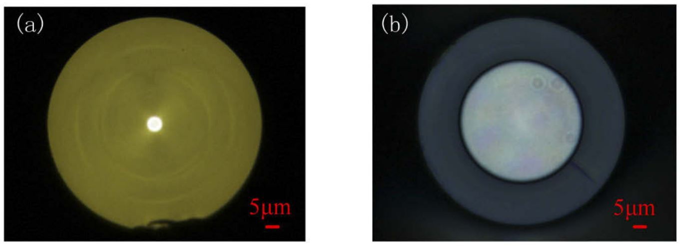

Fig. 4. Microscopic images for the cross section of (a) SMF and (b) hollow-core silica tube (HCST).

waist sizes were fabricated. Their intensity responses were tested in RI liquid. The optimized down-taper had the highest intensity sensitivity, which has a waist diameter of 47.02μm, with tapering length of 307.89μm.

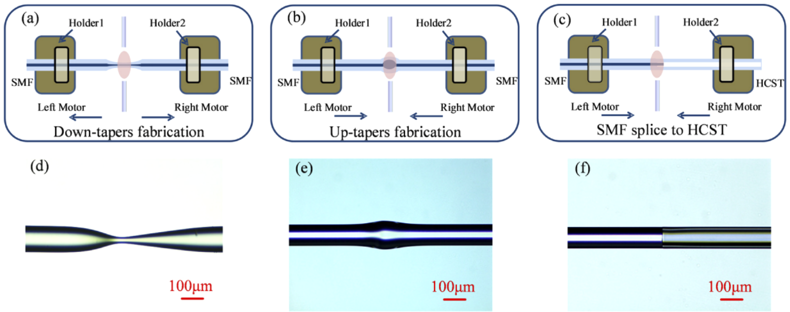

Fig. 5. Schematic picture of (a)SMF down-taper fabrication,(b) SMF up-taper fabrication,(c) SMF splice to HCST in a traditional commercial fusion splicer. Microscopic images of (d) a SMF down-taper, (e) a SMF up-taper (f) the splice joint of SMF (left) and HCST (right).

Table 1. Parameters for tapering SMF and splicing SMF to HCST [30]

Splice parameters	SMF up-taper	SMF down-taper	SMF-HCST
Recipe	SM-SM	SM-SM	MM-MM
Alignment Mode	Core	Core	Cladding
Fiber end face spacing	5μm	Default	Default
overlapping	150μm	Default	10μm
Arc discharge time	Default	1000ms	600ms
Arc discharge intensity	+10 bit	+0bit	-70 bit
Tapersplicemode	Off	On	Off
Tapering speed	Default	+100bit	Default
Tapering length	Default	300μm	Default

Figure 5(d)-(f) display the microscopic pictures of the down-taper, up-taper, and the splice interface between SMF and HCST. The full length of our compact sensor structure is about 10.5 mm. With an optimized HCST length of about 6 mm, a superposition spectrum of multi-beam interference and anti-resonant effect (ARE) can be realized.

In our experiment, a broadband source (BBS, YSL, 900nm-1700nm) is used as the light source, and an optical spectrum analyzer (OSA, YOKOGAWA AQ6370B) is utilized to measure the optical transmission spectrum with 20 pm resolution. The transmission spectrum of the sensor is shown in Fig. 6(a). The large-spaced attenuation dips come from the anti-resonance leakage occurring at resonant wavelengths, while the inset shows the magnified three-beam interference fringe. Similar transmission spectra with identical FSR can be obtained using the same fabrication recipe, confirming the repeatability of the sensor structure. To verify the interference sources of the aforementioned theoretical analysis in our sensor structure, a fast Fourier transform (FFT) algorithm are applied to the transmission spectrum as shown in Fig. 6(b). Three dominant peaks, i.e. 0.7894nm^{-1}, 1.0978 nm^{-1} and 4.8902 nm^{-1}, are obviously observed, which matches well with the pairwise interference in Fig. 6(a). Here, the peak at 1.0978 nm^{-1} represents the interference between light beams in the core and cladding, i.e. I_1 and I_2 in Fig. 1(a). The peak at 4.8902 nm^{-1} is caused by the interference between light beams in the core and the twice-reflection beam, i.e. I_1 and I_3. The peak at 0.7894nm^{-1}comes from the interference between I_2 and I_3.

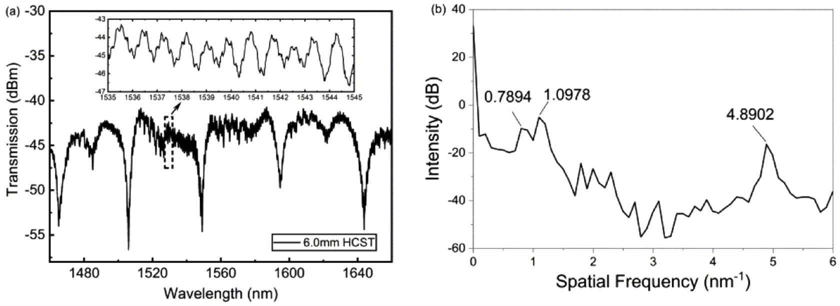

Fig. 6. (a) Transmission spectrum of the sensor. Inset shows the magnified spectrum (in the dash box) of the three-beam interference; (b) Spatial frequency spectra of the sensor.

3.2. Refractive index measurement

For RI measurement, as displayed in Fig. 7, the proposed sensor is placed between two translation stages with each end fixed by fiber holder. A glass slide between the two translation stages is used to support the sensing head during our measurement. The change of ambient RI is realized dripping the refractive index matching fluid (Cargile, Ltd) on the slide, and make sure the sensing part is immersed in the RI liquid.

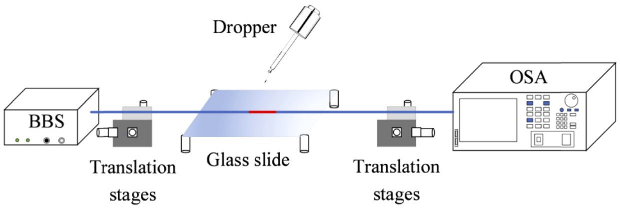

Fig. 7. The experimental setup for measuring external RI. BBS: broadband light source, OSA: optical spectrum analyzer.

The steps for RI measurement are as follows: Firstly, we record the initial spectrum when the sensor is in air. Secondly, we apply the target RI liquid to the sensor. After each dripping, we wait until the spectrum is stable for at least 30 seconds before we record the spectrum. Finally, the sensing head is thoroughly cleaned by ethanol after each measurement. We then wait until the spectrum return to the original status before we take the next RI measurement. Different matching liquids with RI from 1.35 to 1.45 are dropped to the sensor successively. The reason why we used RI liquids instead of artificial samples, i.e. glucose, uric acid, is that the commercial products have calibrated RI values, and also have a wide selection range (1.3 to 1.8) with evenly distributed RI. The RI values of artificial samples rely on the concentration of the solution, which is sensitive to external temperature change.

Figure 8(a) illustrates the experimental transmission spectra of three-beam interference with the external RI changes from 1.35 to 1.45. The results imply that fringe contrast decrease with the increasing RI until it reaches 1.45, which exceeds the RI of silica fiber. Several sensors with different dimensions for down-taper waist: 69µm, 47µm, and 27µm, were tested, with all other sensor parameters the same. We investigated their RI sensing in two aspects: one is the fringe contrast variation, the other is the wavelength response for the anti-resonance dips. All of them showed similar trend as in Fig. 8(a). Nevertheless, the sensor with waist of 47µm gave the highest sensitivity, as shown in Fig. 8(b). From an RI range of 1.35 to 1.43, a highly sensitivity of −120.18 dB /RIU is obtained by demodulating the fringe contrast. It can be seen that the experimental performance of the fringe contrast agrees well with the previous theoretical analysis. Since the attenuation dips caused by anti-resonance are mainly determined by the thickness of the silica tube, the resonance wavelength is barely affected by the external RI. The wavelength response for the dip at 1538 nm is measured to be 3.37 nm/RIU from an RI range of 1.35 to 1.45. To characterize the sensor performance, we fabricated three sensors using the same recipe and conducted the stability, reusability, and reproducibility tests for RI measurements. Our results showed that the average point-to-point fluctuation of the fringe contrast is within 1.5 dB. The reusability measurement was performed by repeating the experiment after thorough cleaning the same sensor probe using alcohol. The uncertainty for the reusability of the optical spectrum is within 5%. For the three sensors, the uncertainty for reproducing the sensitivity of -120.18 dB/RIU is within 6.7%.

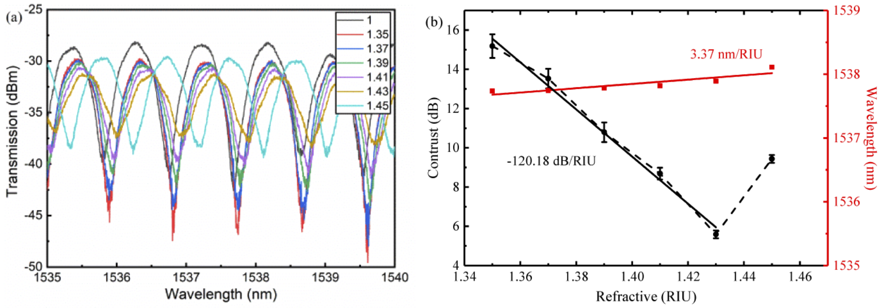

Fig. 8. (a)Transmission spectra of three-beam interference with the external RI changes from 1.35 to 1.45; (b) The fringe contrast (black square) and the wavelength (red circle) response to different RI. Linear fits (red line and black line) indicate RI sensitivities of −120.18 dB/RIU and 3.37 nm/RIU, respectively.

We also performed experiment when replacing the HCST by a MMF with core size of 60µm. Our results show a low sensitivity of 32.7 dB/RIU with 7 nm wavelength shift for an interference dip at around 1441 nm. Result for similar configuration was reported in Ref. [26]. Compared to SMF/MMF structures, higher sensitivity for HCST configurations can be explained by their unique anti-resonant effect, light leakage occurs at or near the resonant wavelengths, which makes the intensity of the transmission dip more sensitive to the external RI change while the resonant wavelength is not. The interference fringes formed by HCST are regularly spaced with small FSR (1 nm). Moreover, the low thermal expansion coefficient for the hollow-core structure potentially allows low temperature cross sensitivity for HCST configurations.

3.3. *Cross sensitivity from temperature*

As we know, temperature stability is of great importance which usually affects the accuracy and precision of sensor measurement. In order to analyze the influence of temperature on the RI measurement, a temperature measurement is performed. The sensor head is placed inside an oven (ECOM, Column oven LCO 102 single, 25~100°C, 0.1°C accuracy) which is an enclosed box (44×47×325 mm) with a removable cover. The oven is tested before the experiment to make sure the entire sensor head is within the area for uniform heating. As we change the temperature at steps of 15°C,the transmission spectra under different temperatures are recorded. For each measurement, we wait for one minute until the spectrum is steady before we move on to the next measurement.

We choose an attenuation dip at around 1535 nm and observe the wavelength as well as intensityvariation when the sensor is exposed in different temperature environment. The results are recorded and plotted, as shown in Fig. 9. The data in red circle represents the wavelength response, indicating a sensitivity of ~30 pm/°C by the linear fitting. The black squares show a small intensity variation of 0.0085 dB/°C. Base on the aforementioned RI measurement data, these results imply an extremely low cross sensitivity of 7×10^{-5} RIU/°C for intensity demodulation, and 0.0089 RIU/°C for wavelength demodulation. This indicates that our sensor has shown

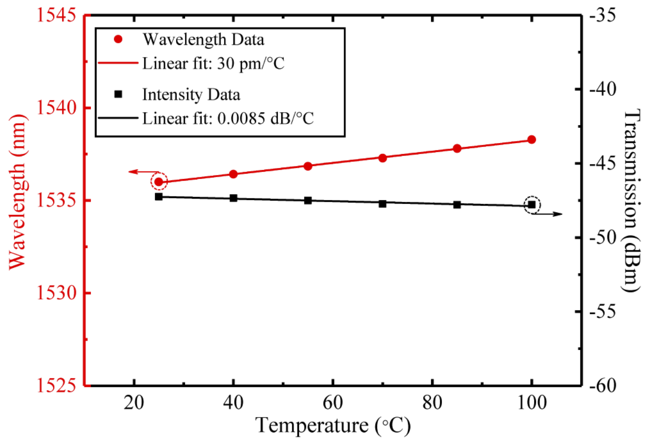

Fig. 9. Linear fitting lines of the observation wavelength versus external temperature, for wavelength (red circle) and intensity (black square) demodulation.

Table 2. Comparison with other published intensity modulated RI sensors

Refs.	Sensing principle	Measurement range	RI sensitivity	Cross sensitivity
[31]	Cascade FP cavity (SMF + HOF + MMF)	1.33-1.45 RIU	16 dB/RIU	None
[32]	FP micro-cavity (SMF + Metal film)	1.30-1.456 RIU	43.59 dB/RIU	None
[33]	Multimode fiber interferometer (SMF + TCF + MMF + SMF)	1.333–1.403 RIU	112.37 dB/RIU	None
[34]	Multimode fiber interferometer (SMF + PCF(taper))	1.333-1.374 RIU	110 dB/RIU	None
[27]	Multimode interferometer (Graphene oxide film)+LPGF	1.312-1.328 RIU	76.32 dB/RIU	None
Our work	Three-beam interference (SMFdown-taper + HCST + SMFup-taper	1.35-1.45 RIU 25-100 °C	120.18 dB/RIU 0.00075 dB/°C	6×10^{-6}RIU/°C

temperature-independent merit which will further benefit its practical application. Table 2 lists the performance of a few fiber-based intensity modulated RI sensors reported. In comparison, our sensor has a higher sensitivity, and also with low temperature cross sensitivity.

4. Conclusions

We propose and fabricate a simple three-beam interferometer for RI sensing based on HCST and SMF tapers. By applying the beam propagation method (BPM), simulation results show that the fringe contrast of the anti-resonance dip in the interference spectrum will vary linearly with the external refractive index in the RI range of 1.35 to 1.43, with a predicted sensitivity of -145 dB/RIU.The experimental result agrees with the simulation, and the measured RI sensitivityreaches up to -120.18 dB/RIU. Furthermore, we also investigated the cross sensitivity from temperature. We found an extremely low cross sensitivity of 7×10^{-5} RIU/°C for dip intensity demodulation, and -0.0085 dB/°C for wavelength demodulation. For certain biosensing applications where fiber sensors are not able to perform an interrogation in transmission, the sensor could be modified in reflection configuration by replacing the SMF up-taper by a thin metal coating with high reflectivity at the end of the HCST. By using just one fiber end, similar interferometer structure can also be obtained. In summary, our sensor's advantages such as simple and compact structure, no requirement of special fibers or techniques, easy to manufacture, immune to external RI changes further benefit its sensing applications in environmental and biochemical fields.

Funding. National Natural Science Foundation of China (61805182).

Disclosures. The authors declare no conflicts of interest.

References

1. D. Wu, Y. Zhao, and J. Li, "PCF taper-based Mach–Zehnder interferometer for refractive index sensing in a PDMS detection cell," Sens. Actuators, B **213**(5), 1–4 (2015).
2. Z. Li, C. Liao, D. Chen, J. Song, W. Jin, G.-D. Peng, F. Zhu, Y. Wang, J. He, and Y. Wang, "Label-free detection of bovine serum albumin based on an in-fiber Mach-Zehnder interferometric biosensor," Opt. Express **25**(15), 17105–17113 (2017).
3. J. M. Zhu, Y. Shi, X. Q. Zhu, Y. Yang, F. H. Jiang, C. J. Sun, W. H. Zhao, and X. T. Han, "Optofluidic marine phosphate detection with enhanced absorption using Fabry-Pérot resonator," Lab Chip **17**(23), 4025–4030 (2017).
4. C. Lin, C. Liao, Y. Zhang, L. Xu, C. Ying Wang, J. KaimingYang, J. He, and Y. Wang, "Optofluidic gutter oil discrimination based on a hybrid-waveguide coupler in fibre," Lab Chip **18**(4), 595–600 (2018).
5. Á. González-Vila, M. Andreas Ioannou, D. Marc Debliquy, and C. Caucheteur, "Surface plasmon resonance sensing in gaseous media with optical fiber gratings," Opt. Lett. **43**(10), 2308–2311 (2018).
6. Z. Zhang, J. He, B. Du, K. Guo, and Y. Wang, "Highly sensitive gas refractive index sensor based on hollow-core photonic bandgap fiber," Opt. Express **27**(21), 29649–29658 (2019).
7. X. Yang, S. Wu, H. Cheng, J. Ma, S. Wang, S. Liu, and P. Lu, "Simplified highly-sensitive gas pressure sensor based on harmonic Vernier effect," Opt. Laser Technol. **140**, 107007 (2021).
8. S. C. Warren-Smith and T. M. Monro, "Exposed core micro-structured optical fiber Bragg gratings: refractive index sensing," Opt. Express **22**(2), 1480–1489 (2014).
9. L. Rindorf and O. Bang, "Highly sensitive refractometer with a photonic-crystal-fiber long-period grating," Opt. Lett. **33**(6), 563–565 (2008).
10. T. Guo, F. Liu, B. Guan, and J. Albert, "Polarimetric multi-mode tilted fiber gratingsensors," Opt. Express **22**(6), 7330–7336 (2014).
11. B. Shuai, L. Xia, Y. Zhang, and D. Liu, "A multi-core holey fiber based plasmonic sensorwith large detection range and high linearity," Opt. Express **20**(6), 5974–5986 (2012).
12. Y. Zhang, C. Zhou, L. Xia, X. Yu, and D. Liu, "Wagon wheel fiber based multichannelplasmonic sensor," Opt. Express **19**(23), 22863–22873 (2011).
13. Q. Wang, L. Kong, Y. Dang, F. Xia, Y. Zhang, Y. Zhao, H. Hu, and J. Li, "High sensitivity refractive index sensor based on splicing points tapered SMF-PCF-SMF structure Mach-Zehnder mode interferometer," Sens. Actuators, B **225**, 213–220 (2016).
14. W. He, Y. Fang, L. Zhu, M. Dong, X. Lou, and F. Luo, "Optical fiber interference sensor based on fiber ending micro-groove fabricated by femtosecond laser," Optik **158**, 1295–1301 (2018).
15. C. Viphavakit, S. O'Keeffe, M. Yang, S. Andersson-Engels, and E. Lewis, "Gold Enhanced Hemoglobin Interaction in a Fabry-Perot Based Optical Fiber Sensor for Measurement of Blood Refractive Index," J. Lightwave Technol. **36**(4), 1118–1124 (2018).

16. C. Wang, W. Jin, C. Liao, J. Ma, W. Jin, F. Yang, H. L. Ho, and Y. Wang, "Highly birefringent suspended-core photonic microcells for refractive-index sensing," Appl. Phys. Lett. **105**(6), 061105 (2014).
17. Y. Zheng, L. H. Chen, X. Dong, J. Yang, H. Y. Long, P. L. So, and C. C. Chan, "Miniature pH Optical Fiber Sensor Based on Fabry-Perot Interferometer," IEEE J. Sel. Top. Quantum Electron. **22**(2), 331–335 (2016).
18. F. Long, A. Zhu, H. Shi, H. Wang, and J. Liu, "Rapid on-site/in-situ detection of heavy metal ions in environmental water using a structure-switching DNA optical biosensor," Sci. Rep. **3**, 2308 (2013).
19. M. E. Muthuraju, A. R. Patlolla, B. V. Canthadai, and V. Pachava, "Low cost fiber optic sensing of sugar solution," Proc. SPIE **9317**, 93170L (2015).
20. Q. F. Ma, Z. Q. Tou, K. Ni, Y. Y. Lim, Y. F. Lin, Y. R. Wang, M. H. Zhou, F. F. Shi, L. Niu, X. Y. Dong, and C. C. Chan, "Carbon-nanotube/Polyvinyl alcohol coated thin core fiber sensor for humidity measurement," Sens. Actuators, B **257**, 800–806 (2018).
21. J. Ma, S. Wu, H. Cheng, X. Yang, S. Wang, and P. Lu, "Sensitivity-enhanced temperature sensor based on encapsulated S-taper fiber Modal interferometer," Opt. Laser Technol. **139**, 106933 (2021).
22. S. Wand, S. Liu, W. Ni, S. Wu, and P. Lu, "Dual-wavelength highly-sensitive refractive index sensor," Opt. Express **25**(13), 14389–14396 (2017).
23. C. Jiang, Y. Liu, Y. Zhao, C. Mou, and T. Wang, "Helical Long-Period Gratings Inscribed in Polarization-Maintaining Fibers by CO2-Laser," J. Lightwave Technol. **37**(3), 889–896 (2019).
24. Z. Zhang, T. Guo, and B. Guan, "Reflective Fiber-Optic Refractometer Using Broadband Cladding Mode Coupling Mediated by a Tilted Fiber Bragg Grating and an In-Fiber Mirror," J. Lightwave Technol. **37**(11), 2815–2819 (2019).
25. Q. Wang, B. sun, E. Hu, and W. Wei, "Cu/ITO coated uncladded fiber-optic biosensor-based on surface plasmonresonance," IEEE Photonics Technol. Lett. **31**(14), 1159–1162 (2019).
26. J. Kang, J. Yang, X. Zhang, C. Liu, and L. Wang, "Intensity Demodulated Refractive Index Sensor Based on Front-Tapered Single-Mode-Multimode-Single-Mode Fiber Structure," Sensors **18**(7), 2396–2404 (2018).
27. M. Shao, X. Qiao, H. Fu, H. Li, Z. Jia, and H. Zhou, "Refractive Index Sensing of SMS Fiber Structure Based Mach-Zehnder Interferometer "IEEE Photon," IEEE Photonics Technol. Lett. **26**(5), 437–439 (2014).
28. S. Liu, J. Tian, S. Wang, Z. Wang, and P. Lu, "Anti-Resonant Reflecting Guidance in Silica Tubefor High Temperature Sensing," IEEE Photonics Technol. Lett. **29**(23), 2135–2138 (2017).
29. H. Cheng, S. Wu, Q. Wang, S. Wang, and P. Lu, "In-Line Hybrid Fiber Sensor for Curvature and Temperature Measurement," IEEE Photonics J. **11**(6), 1–11 (2019).
30. S. Kumar, R. Singh, B. K. Kaushik, N. Chen, Q. S. Yang, and X. Zhang, "LSPR-Based Cholesterol Biosensor Using Hollow Core Fiber Structure," IEEE Sens. J. **19**(17), 7399–7406 (2019).
31. H. Y. Choi, G. Mudhana, K. S. Park, B. H. Un-ChulPaek, and Lee, "Cross-talk free and ultra-compact fiber optic sensor for simultaneous measurement of temperature and refractive index," Opt. Express **18**(1), 141–149 (2010).
32. C. L. Lee, J. M. Hsu, J. S. Horng, W. Y. Sung, and C. M. Li, "Microcavity Fiber Fabry-Pérot Interferometer With an Embedded Golden Thin Film," IEEE Photonics Technol. Lett. **25**(9), 833–836 (2013).
33. Y. Zhao, F. Xia, and J. Li, "Sensitivity-Enhanced Photonic Crystal Fiber Refractive Index Sensor With Two Waist-Broadened Tapers," J. Lightwave Technol. **34**(4), 1373–1379 (2016).
34. M. Singh, S. K. Raghuwanshi, and O. Prakash, "Ultra-Sensitive Fiber Optic Gas Sensor Using Graphene Oxide Coated Long Period Gratings," IEEE Photonics Technol. Lett. **31**(17), 1473–1476 (2019).